Engineering 49 (2025) 113–121

Contents lists available at ScienceDirect

Engineering

journal homepage: www.elsevier.com/locate/eng

Research
Laser Micro/Nano-Manufacturing—Article

Fish Skin Inspired Scale Armored Sliding Surfaces

Jialiang Zhang [a], Qing Yang [b,*], Qingyun Ma [a], Fangzheng Ren [a], Yang Cheng [b], Xiaodan Gou [a], Jie Liang [a], Feng Chen [a,*]

[a] State Key Laboratory for Manufacturing System Engineering & Shaanxi Key Laboratory of Photonics Technology for Information, School of Electronic Science and Engineering, Xi'an Jiaotong University, Xi'an 710049, China
[b] School of Instrument Science and Technology, Xi'an Jiaotong University, Xi'an 710049, China

ARTICLE INFO

Article history:
Received 14 November 2023
Revised 13 August 2024
Accepted 6 September 2024
Available online 14 November 2024

Keywords:
Fish skin
Sliding surface
Femtosecond laser
Mechanical sturdiness
Scale armor

ABSTRACT

Hard scales in scaly fish species ensure the structural and functional integrity of the inner skin and body, even when subjected to various types of external forces. Mucus and oil secreted from the inner layer of the fish skin to the surface exhibit resistance to a wide range of liquids, maintaining the antifouling properties of the fish skin surface. Inspired by these biological structures, ultra-sturdy and durable scale-armored-sliding surfaces (SASSs) were fabricated in this study using femtosecond laser electrodeposition (FED). In the FED method, a scaly structure is grown from the substrate across a sliding layer to form an SASS. The unique scale-armored structure offers protection against impact and abrasion while maintaining the performance and integrity of the structure. The mechanical sturdiness of the SASS improved by four orders of magnitude compared to that of the conventional antifouling surface. In addition, the SASS exhibited remarkable chemical durability, excellent hydraulic pressure resistance, liquid repellency, and good corrosion resistance based on characterization using various methods. FED enables the preparation of SASS on several materials, including Cu and Al and more. SASS fabricated using FED has great potential for the application of antifouling surfaces in extremely harsh environments.

1. Introduction

After millions of years of evolution, diverse fish species have developed scales of varying shapes. Irrespective of the fish type or scale morphology, these scales play a crucial role in shielding the tender skin from numerous abrasions and shocks [1,2]. They serve as protective barriers to the inner skin and body, even in the harshest natural environments. In addition, these scales facilitate proper functioning of the inner skin, aiding the secretion of mucus or oil onto the surface of the scales [3,4]. Mucus or oil secreted by the inner skin on the surface of the fish scales forms the epidermal layer. This layer ensures prolonged antifouling of the surface, enabling fish to maintain clean skin, even in extremely filthy environments [5].

Recently, bioinspired slippery surfaces have gained significant attention [6–8]. On slippery surfaces, a lubricant is infused into the porous structure of the surfaces or a polymer network substrate, spontaneously forming a perfectly smooth interface that effectively prevents exterior fouling. Generally, the behavior of a droplet on these surfaces remains consistent with a very small sliding angle (SA) because the slippery nature significantly reduces the friction between the droplet and the surface [9]. This property allows the droplet to slide off the surface at a slight angle owing to gravity. Bioinspired slippery surfaces are highly effective against various pollutants, including viscous liquids, bacteria, and external pollutants [10]. In addition, slippery surfaces can maintain antifouling properties that are not affected by liquid type, humidity, or hydraulic pressure [11–13]. These slippery antifouling surfaces have potential for applications in corrosion resistance, icing prevention, and safeguarding device surfaces to ensure normal operations [14–16]. Globally, trillions of dollars are spent on corrosion resistance each year [17]. Existing methods for preparing slippery antifouling surfaces include chemical etching, hydrothermal, anodic oxidation, particle coating, and laser ablation [18–26]. Ouyang et al. [27] used electrodeposition to create a micro-nanostructure on an Mg–Li alloy surface and filled it with oil gel, which significantly improved its corrosion resistance. The surface maintained strong corrosion resistance even after 30 days in an

* Corresponding authors.
E-mail addresses: yangqing@mail.xjtu.edu.cn (Q. Yang), chenfeng@mail.xjtu.edu.cn (F. Chen).

https://doi.org/10.1016/j.eng.2024.09.026

NaCl solution. Cheng et al. [28] fabricated a slippery liquid-infused porous surface on the surface of a TiNi alloy using a femtosecond Bessel laser with antifouling properties, including antibacterial and anticell adhesion. Although slippery antifouling surfaces can be prepared using these methods, their long-term durability is limited. These slippery antifouling surfaces cannot guarantee their wettability for prolonged periods in the case of structural integrity or lose their antifouling ability owing to external damage to the structure [29–31]. However, in complex and harsh environments, these antifouling surfaces must exhibit significant mechanical sturdiness and good chemical durability to maintain their structural integrity and slippery performance for extended periods [32–35]. This is a drawback to the development of antifouling surfaces [36,37]. Developing an appropriate method for fabricating antifouling surfaces with good mechanical sturdiness and chemical durability could substantially contribute to economic and energy savings. Cultivating rigid scales on slippery antifouling surfaces that are akin to those found on fish skin may be a promising approach to overcoming these deficiencies. Such scales have the potential of improving mechanical sturdiness and ensuring sustained exceptional antifouling performance. This approach can potentially overcome significant hurdles in the advancement of highly sturdy antifouling surfaces [38,39].

In this study, inspired by the fish skin structure, an ultra-sturdy and durable antifouling surface called scale-armored-sliding surface (SASS) was fabricated using a new manufacturing method named femtosecond laser electrodeposition (FED), which exhibits excellent mechanical sturdiness and chemical durability. The FED method enables scales and a sliding layer to intertwine, resembling a fish skin design. A sturdy scale structure protected the fragile sliding layer from impact and abrasion. Compared with conventional antifouling surfaces, SASS improves the impact resistance by four orders of magnitude and the abrasion resistance by three orders of magnitude. The shape of the scale can be adjusted as required, with minimal influence on its mechanical sturdiness. The SASS exhibited excellent chemical durability based on the results of various tests, including the liquid resistance of composite liquids and droplets at different pH values, hydraulic pressure, salt spray, electron impedance spectroscopy (EIS), and Tafel curve tests. The new SASS structure prepared using the FED method exhibits superior mechanical sturdiness and chemical durability, which significantly extends the applicability of slippery antifouling surfaces.

2. Experiment

2.1. Fabrication of SASS

First, a metal sample (Dongguan Yuexin Metal Materials Co., Ltd) was encapsulated in an epoxy resin (JINHUA Materials, China). One side of the encapsulated metal was polished using sandpaper (#1000) and a polishing machine. Next, the sliding layer is prepared; the prepolymer and curing agent (Sylgard 184, Dow Corning, USA) were mixed at a ratio of 10:1 to produce polydimethylsiloxane (PDMS). Silicone oil (Shanghai Aladdin Biochemical Technology, China) and PDMS were then mixed in a ratio of 1.1:1; this mixture was spin-coated onto the surface of the encapsulated metal sample and cured in a drying oven at 60 °C for 2 h. After covering the sliding layer, the sample was processed and ablated using a femtosecond laser galvanometer system (Siemens Str 2a 82178 Puchheim, SCANLAB, Germany). A laser beam (50 fs, 800 nm, and 1 kHz) was generated using a Ti:sapphire laser system (Libra-usp-he, Coherent, USA) guided to the galvanometer system. The laser power was maintained at 200 mW, and the ablation speed of the laser was 8 $mm \cdot s^{-1}$. The adjacent distance (AD) of laser scanning was adjusted to 8 μm in each square ablation hole. After laser processing, the samples were sequentially cleaned ultrasonically with alcohol and distilled water (CJ-G040SST, SCJ Inc., China). Subsequently, an electrochemical workstation (CS350M, CORRTEST, China) was used for deposition. The sample was connected to a counter electrode, and the working and reference electrodes were connected to a Cu rod. The Cu rod (Dongguan Yuexin Metal Materials Co., Ltd.) was placed opposite to the sample in a 5 wt% $CuSO_4$ solution. The steady-state current polarization mode was selected for the electrochemical workstation. The polarization current was 70 mA, and the polarization time was 40 min. During the deposition process, the electrolyte solution was stirred using magnetic beads. The hole bottom of the sample ablated by the femtosecond laser was the negative electrode, and the released electrons attracted the Cu ions in the solution to reduce them to Cu at the porous bottom and rise upward along the wall of the ablated hole. As the positive electrode, the Cu rod continuously lost electrons and released Cu ions into the electrolyte solution. After deposition, the sample was washed with distilled water. The sample was then placed in silicone oil to enable the SASS to absorb the lubricant. After 24 h, SASS was prepared.

2.2. Characterization of SASS

The SASS was characterized via structural, wettability, mechanical stability, and chemical characterization. The details of the SASS characterization are presented in Section S1 in Appendix A.

3. Results and discussion

3.1. Design strategy of SASS

Fish skin has an exceptional antifouling function and effectively resists adhesion of various liquids. This protects the skin surface from potential external environmental pollutants. Furthermore, owing to the protective property of hard scales, fish skin can mitigate external impact and abrasion, thereby preserving the integrity of the delicate inner skin [40,41]. A simplified model was derived from scaly fish skin structures. The supple skin surface is adorned with rigid scales, whereas the inner skin secretes mucus or oil, which in turn, covers the layer of scales (Fig. 1(a)). These scales play a pivotal role in protecting tender inner layers of the skin. Inspired by this biological fish skin structure, the scales were incorporated into an antifouling sliding layer, culminating in the development of an SASS (Fig. 1(b)). The scales were then integrated into the substrate. The sliding layer exhibited outstanding liquid repellency, whereas the vulnerable structure of the layer was easily destroyed or peeled off by impact or abrasion. The SASS exhibited the same antifouling properties as the sliding layer. However, the structural integrity and slippery performance were maintained even after subjecting the surface to a strong external impact or abrasion, owing to the protection by the sturdy scales. The scales were integrated with the subject across the sliding layer. The bottom of the scales was connected to the inside of the substrate, and the top edge was wrapped outward around the top-layer surface (Fig. 1(c)). The scales were staggered to ensure that the sliding layer did not separate from the scales. This interlocked solid structure can withstand thousands of impact and abrasion cycles while maintaining the structural and performance integrity of the inner soft-sliding layer, similar to a scaly fish. Fig. 1(d) shows a cross-section of the SASS structure. The thickness of the sliding layers was approximately 70 μm. When the surface was subjected to an external force, no stress distribution was observed around the sliding layer, and all the stresses were concentrated in the scaled area (Fig. 1(e)). In the side view, the stress was distributed along

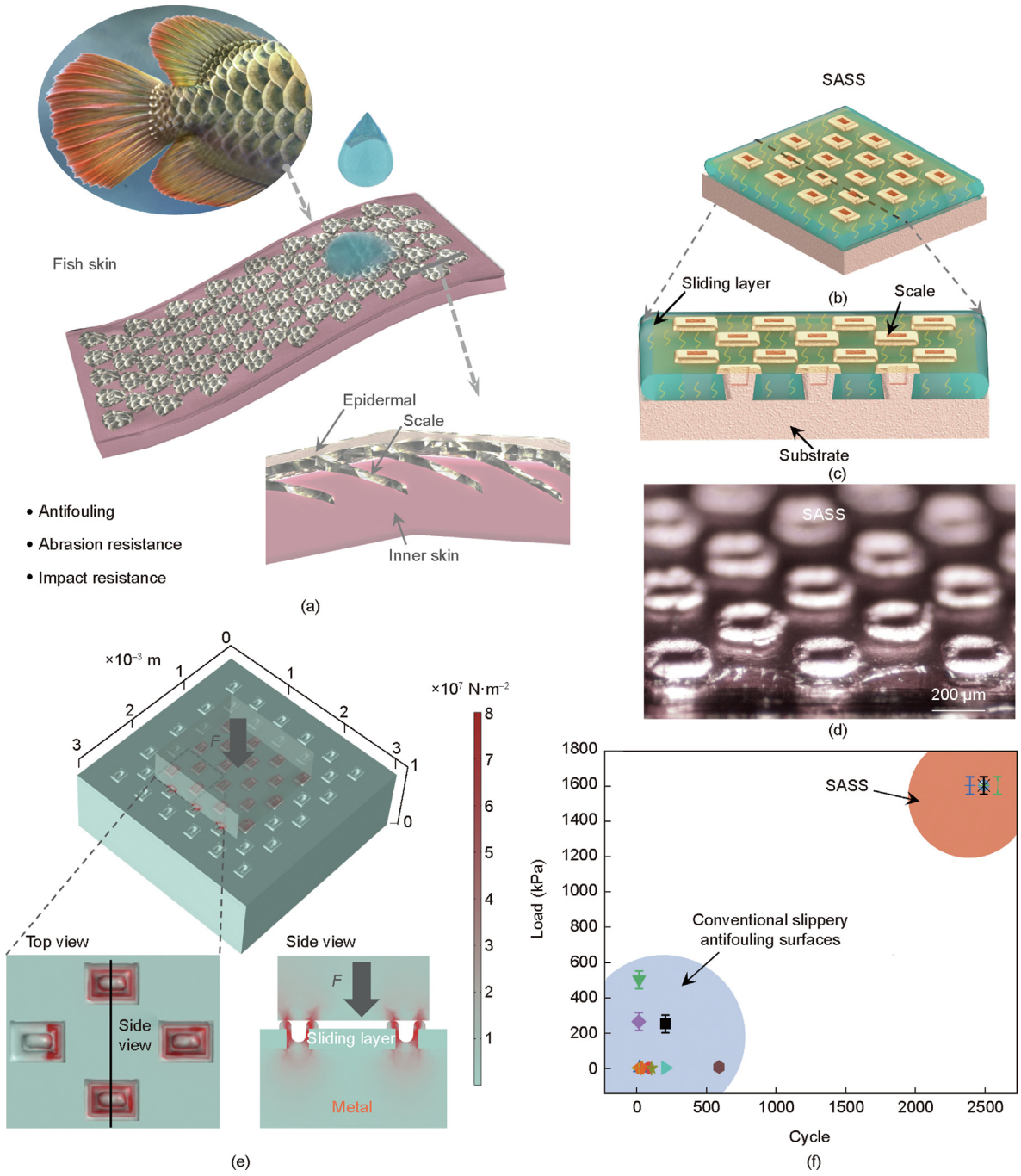

Fig. 1. The SASS design strategy. (a) Scaly fish skin and a simplified model of the skin structure. (b) Schematic of SASS. (c, d) Schematic and photograph of SASS cross-section. (e) Numerical simulation results of the surface stress distribution of SASS under an external force (*F*). (f) Comparison of the mechanical sturdiness between a conventional slippery antifouling surface and SASS.

the scale from the top of the scale to the solid substrate, and the top layer adjacent to the scale was not stressed. In other words, the solid substrate also resisted pressure, which is the reason for the exceptional mechanical sturdiness of the SASS. Fig. 1(f) shows a comparison between the abrasion resistance of the SASS and conventional slippery antifouling surface, where the blue area represents the conventional slippery antifouling surface, and the orange area represents the SASS [42–51]. On the basis of the number of abrasion loads and cycles, the performance of the SASS significantly exceeded that of conventional antifouling surfaces, as shown in Fig. S1 in Appendix A. A sample comprising half SASS and half pure-sliding layers was subjected to the same hammer impact, tweezer scratching, and blade scratching. The SASS maintained its structural integrity and antifouling performance, whereas the pure-sliding layer lost its entire antifouling property owing to the peeling of the top layer (Movie S1 in Appendix A).

3.2. FED method and structure of SASS

Fig. 2(a) shows the FED fabrication process. Subtractive (femtosecond laser ablation) and additive (electrodeposition) manufacturing were performed sequentially on the sliding layer. A sliding layer consisting of PDMS and silicone oil was coated onto the substrate. This polymer sliding layer can store the lubricant in its

molecular chain by soaking it in silicon oil after curing. During use, oil was continuously secreted from the sliding layer onto the surface. After coating the metal substrate with a sliding layer, the through-holes across the PDMS substrate were ablated using a femtosecond laser. The ablation holes were conical and directly penetrated the top layer into the interior of the metal substrate. During ablation, the femtosecond laser slightly detached from the focus as the hole depth increased, causing the bottom area of the hole to become smaller than the top area of the hole. The top of the rectangular hole was approximately 200 μm × 130 μm (Fig. 2(b)). During electrodeposition, metal ions in the electrolyte were reduced inside the bottom of the holes, and the scale structure grew upward along the hole and was connected to the metal substrate by metallic bonds. Because of the edge effect of electrodeposition, the deposition rate at the bottom of the hole was higher than that at the wall of the hole. The metal deposited at the bottom integrated with the metal substrate, and the metal at the edge of the hole grew upward along the hole wall. The top of the scales wrapped around the edges of the ablation holes within a specific electrodeposition time, and thus, the top layer was embedded in the scales. The results of the electrodeposition process simulation show the change in the deposition thickness on the sidewall of the hole with deposition time (Fig. 2(c)). By measuring and comparing the outline of the hole after ablation and electrodeposition, the deposited metal at the bottom was found to be the thickest, which was consistent with the simulation results, indicating that the scales, sliding layer, and substrate were tightly bonded together (Fig. 2(d)). Lubricant was infused into the sliding layer by immersing the surface in the lubricant. This sequence of processes was followed to fabricate the SASS.

Because of the flexibility of femtosecond laser processing, scales can be adjusted to various shapes during the femtosecond laser ablation process, including, but not limited to, rectangles, circles, triangles, and roundness. The surface morphology of the rectangular scale is shown in Fig. 2(e), where the top of the scale length and width are approximately 200 and 150 μm, respectively. The elemental distributions are shown in Fig. 2(f), where Si represents the sliding layer, and Cu represents the scales. A three-dimensional SASS structure is shown in Fig. 2(g), where the scales are higher than the sliding layer by approximately 40 μm. The middle part of the scale has a concave structure that reduces the contact between the droplets and the top of the scale and stores the lubricant during infusion. The scale structure and sliding layer were intertwined on the SASS surface. The scale area is based on the area of the femtosecond-laser-ablated holes in the self-lubricating layer, which occupies a specific area of the sliding layer in the SASS structure. Therefore, the mechanical sturdiness was analyzed for different scale ratios to the total area of 0–30%. Here,

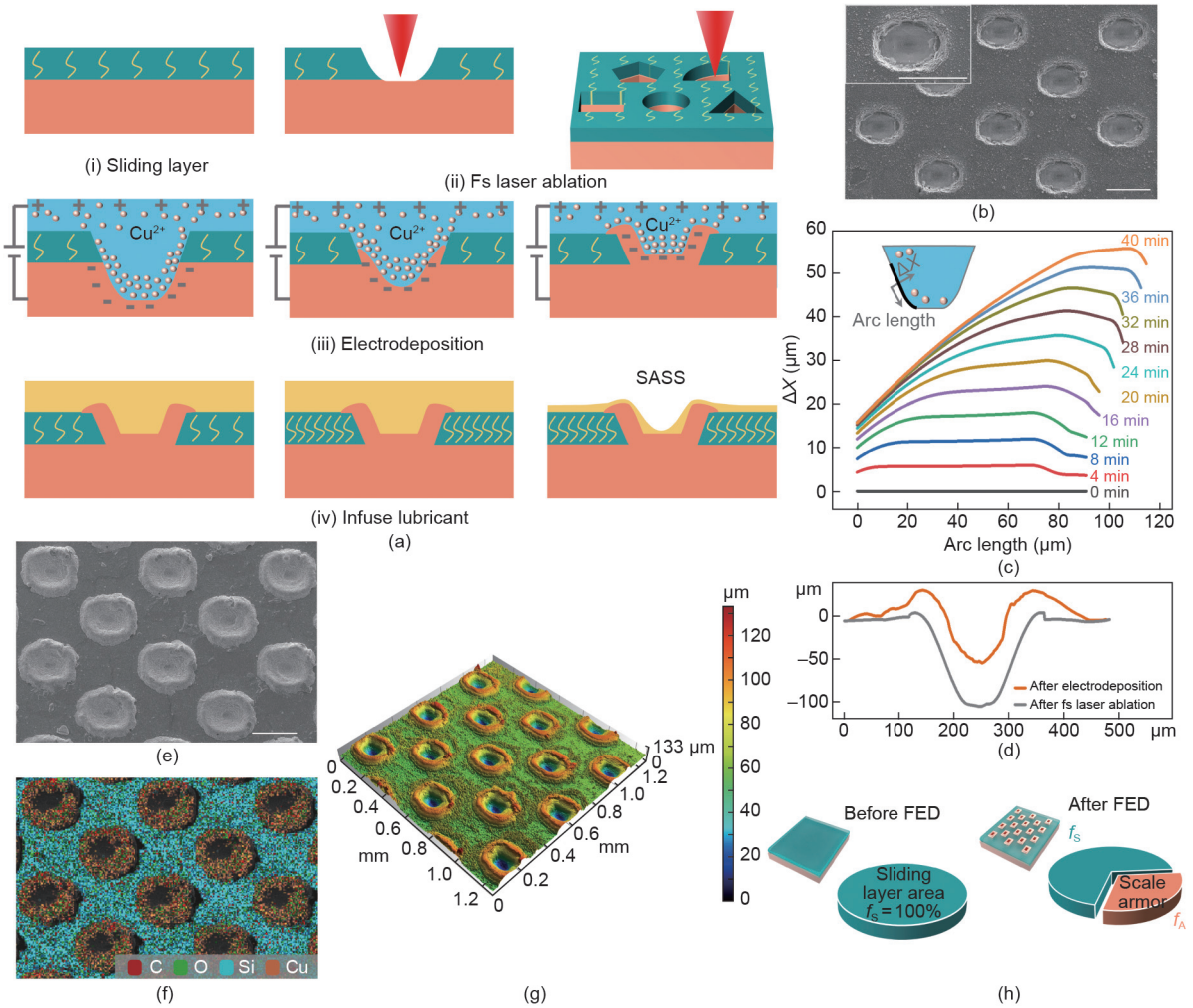

Fig. 2. (a) FED fabrication process. (b) Surface morphology after femtosecond laser ablation (scale bar: 200 μm). (c) Simulation results for variation in thickness on ablation side wall with electrodeposition time. (d) Outline after femtosecond ablation and after electrodeposition. (e) Surface morphology of SASS (scale bar: 200 μm). (f) Surface elemental distribution corresponding to (e), (scale bar: 200 μm). (g) Three-dimensional structure of SASS. (h) f_S and f_A before and after FED. fs: femtosecond.

f_A is the area ratio of the scale armor, which is defined as the ratio of the ablation area, and f_S is the area ratio of the sliding layer (Fig. 2(h)).

3.3. Mechanical stability of SASS

Different f_A values (0–30%) were analyzed with respect to the mechanical sturdiness of the SASS, including impact and abrasion cycles (Fig. 3). During the impact cycle tests, a steel probe repeatedly hit the SASS surface under a force of 200 N. In the impact cycle test setup (Fig. 3(a)), the top of the probe was a 10 mm × 10 mm rectangular plane, indicating that the pressure of each impact exceeded 2 MPa, as shown in Movie S2 in Appendix A. Fig. 3(b) shows the sliding time of the droplets on the surface after the impact cycles. The surface tilt angle was 20°, and the droplet volume was 40 μL. At an ablation ratio f_A = 0, the pure-sliding layer lost its wettability after one impact cycle because its structure was completely destroyed. With an increase in f_A, the number of cycles initially increased but then decreased. When f_A increased, f_S decreased, and lubricant storage correspondingly decreased. The number of cycles represents the critical value for the balance between surface wettability and mechanical sturdiness. Once the

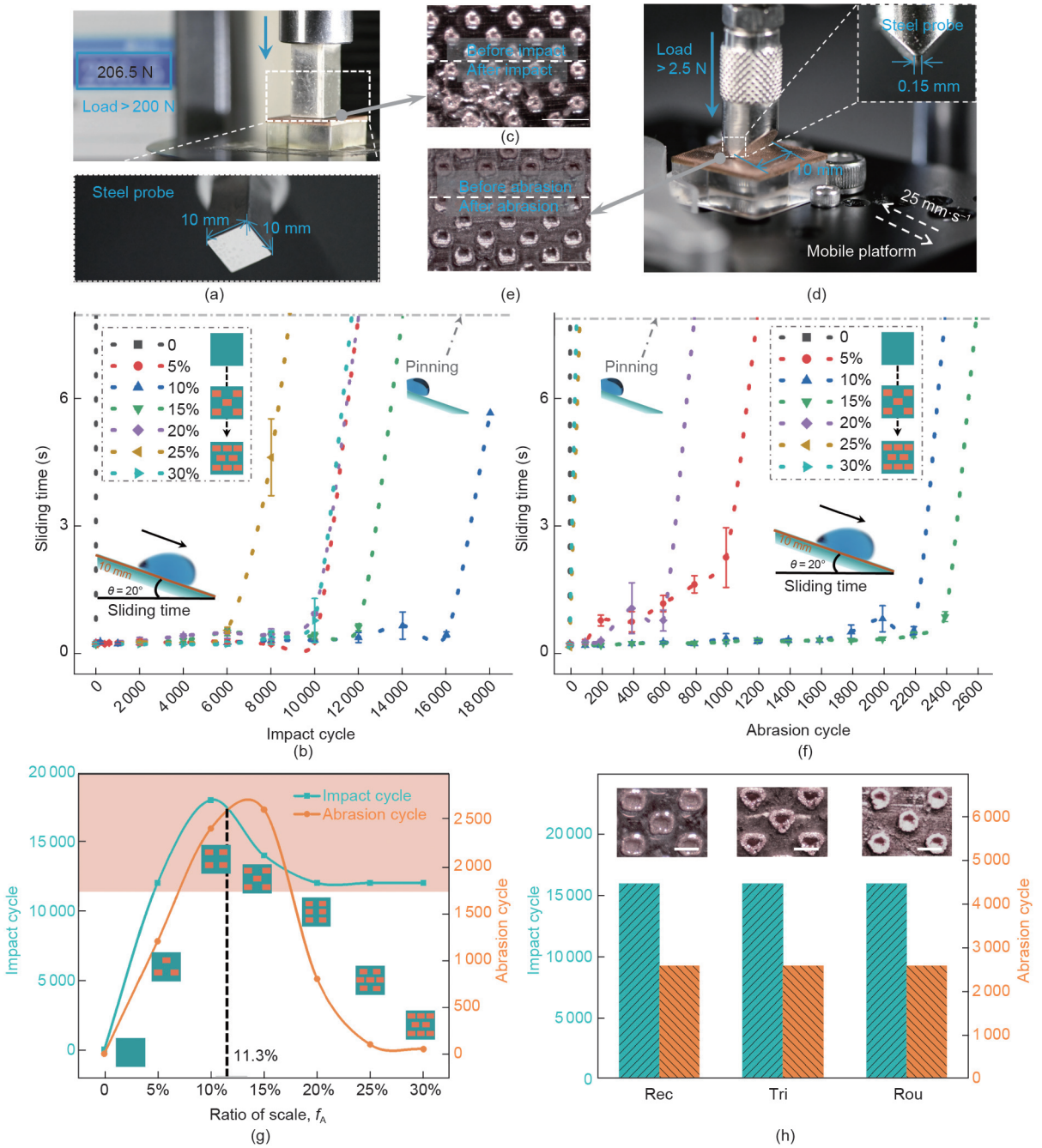

Fig. 3. Mechanical sturdiness tests on SASS with different f_A values. (a) Impact cycle test setup. (b) Impact cycles of SASS with different f_A values, which is represented by the droplet sliding time on the SASS after impact cycles. The slope length is 10 mm, and the angle is 20°. (c) SASS surface before and after impact cycle tests (scale bar: 5 mm). (d) Abrasion cycle test setup. (e) SASS surface before and after abrasion cycle tests (scale bar: 5 mm). (f) Abrasion cycles of the SASS with different f_A values. (g) Variations in abrasion resistance and impact resistance of the SASS with f_A. (h) Impact resistance and abrasion resistance of SASS with different scale shapes (rectangular (Rec), triangular (Tri), and roundness (Rou)) (scale bar: 200 μm).

number of cycles exceeded this critical value, the droplets were pinned to the surface, indicating a loss of antifouling characteristics. The f_A value of 10% yielded the best impact resistance, and the surface lost its antifouling property after 18 000 impact cycles. The change in the contact angle (CA) was slight, within the range of 20°, as shown in Fig. S2 in Appendix A. The top of the scales resisted the entire impact force, protecting the fragile sliding layer from damage. The impact area was relatively flat owing to the flat impact probe. After 18 000 impact cycles, the surface structure at f_A = 10% was partially damaged, which led to a loss of liquid resistance (Fig. 3(c) and Fig. S2). Abrasion resistance tests were performed using SASS with different f_A values.

A load greater than 2.5 N was used in the test setup, indicating that the pressure during abrasion exceeded 1.67 MPa (Fig. 3(d)). During the abrasion test, a steel probe was abraded 17 mm back and forth on the SASS (Movie S3 in Appendix A). The abraded area was located between the scale armor and the abrasion probe without abrasion of the sliding area when undergoing abrasion cycles on SASS with different f_A values (Fig. 3(e)). The best abrasion resistance was achieved for f_A = 15% after 2600 cycles (Fig. 3(f)). The CA ranged from 95° to 105° and slightly increased with the number of abrasion cycles (Fig. S3 in Appendix A). The surface morphology of the SASS at f_A = 15% after 2600 abrasion cycles showed visible scratches in the abrasion direction at the top of the scale armor in the abrasion area. All the abrasion traces were borne by the scale armor structure; therefore, the sliding layer structure was maintained (Fig. S3 in Appendix A). The droplets could not slide on the surface because the worn-out scale armor exposed the hydrophilic intrinsic metal surface. The number of abrasion cycles and the hydrophilic area increased with increasing f_A. The SASS must show a balance between impact resistance and abrasion resistance. This balance was achieved at f_A = 11.3% (Fig. 3(g)). The mechanical sturdiness of different scale shapes at f_A = 11.3% was investigated with respect to the impact resistance and abrasion resistance. The scales were triangular, rectangular, and roundness. The SASS with the same f_A and different scale shapes exhibited similar mechanical sturdiness, including impact and abrasion resistance (Fig. 3(h)). The three shapes had the same ablation area during fabrication. The impact resistance attained 16 000 cycles, each with an impact pressure of 2 MPa, and the abrasion resistance achieved 2600 cycles, each with an abrasion pressure of 1.6 MPa (Fig. S4 in Appendix A).

Fig. 4 shows the changes in wettability of SASS with different scale shapes determined from the impact and abrasion tests. In

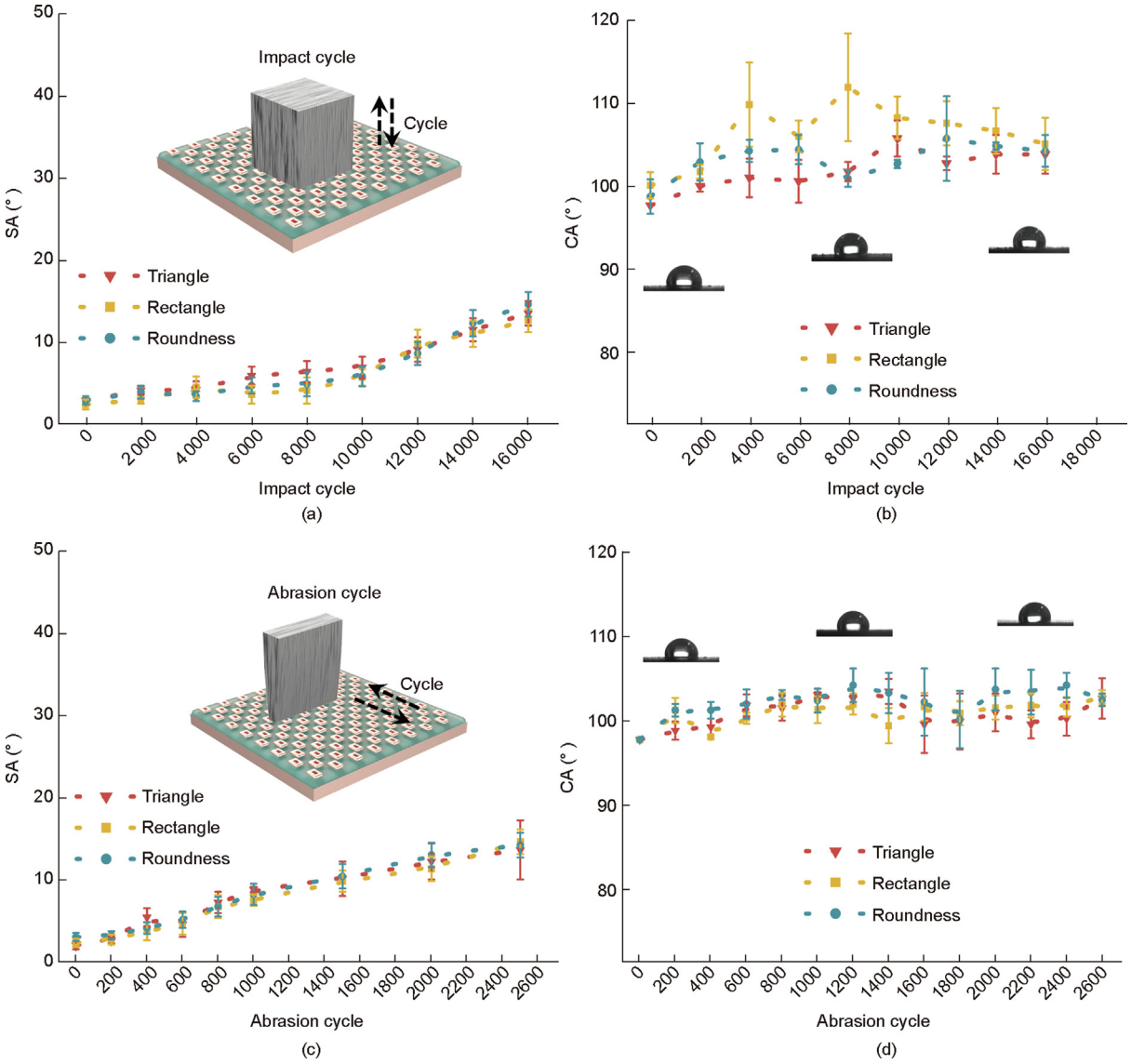

Fig. 4. Changes in wettability of SASS with three scale shapes during impact and abrasion tests. (a) SA during the impact test. (b) CA during the impact test. (c) SA during the abrasion test. (d) CA during the abrasion test. Droplet volume: 10 μL.

the tests, a droplet with a volume of 10 μL was applied. During the impact test, the SA of the SASS with the three scale shapes changed from 3° to approximately 15° after 16 000 impact cycles, with each cycle subjected to an impact pressure of 2 MPa (Fig. 4(a)). The CA ranged from 100° to 110° before and after the impact test (Fig. 4(b)). For the abrasion test, the SA of the SASS with three scale shapes changed from 3° to approximately 16° after 2500 abrasion cycles (Fig. 4(c)), with 1.6 MPa pressure applied in each abrasion cycle. The CA slightly varied during the abrasion test, ranging from 100° to 105° (Fig. 4(d)). The morphologies of the different scale shapes after impact and abrasion showed that the sliding layer structure was damaged after the scale armor was destroyed (Figs. S5 and S6 in Appendix A). These results indicate that the shape of the scale minimally influenced the mechanical sturdiness; the dominant factor was f_A, which was 11.3% in this case. A corresponding numerical simulation was performed to reveal the mechanism of the SASS with such excellent mechanical sturdiness. When the surface experienced external pressure, the scale armor resisted all stresses, indicating stress distribution on the solid substrate (Fig. S7 in Appendix A). This is because the hard scales bore all the stress, which were transmitted longitudinally along the scale structure to the rigid substrates. In other words, the outer hard scales and the inner rigid substrate protected the soft sliding layer of the surface from damage. A soft sliding layer with no stress distribution can maintain its liquid repellency and self-cleaning performance, even after thousands of external abrasion loading cycles. In addition, the SASS exhibited excellent self-recovery behavior because the lubricant could be secreted from within the sliding layer to the surface during the polypropylene (PP) probe abrasion test. Following the antifouling performance failure of the SASS during the PP probe abrasion test, the slippery performance fully recovered within 24 h, demonstrating its exceptional self-recovery ability (further details are provided in Section S2 and Fig. S8 in Appendix A).

3.4. Chemical durability of SASS

FED can be applied to many metals to fabricate SASS, including Cu, Al, Ni, stainless steel, Ti, and TiNi alloys. Figs. 5(a)–(f) shows these entities and their structures. These SASS exhibited similar antifouling performances, including sliding time and CA. The sliding time was approximately 0.2 s for a tilt surface angle of 20°, sliding distance of 10 mm, and droplet volume of 40 μL. The CA values were approximately 100° (Fig. 5(g)). These results suggest that FED is a universal and effective technique for fabricating SASS on different metal substrates, significantly expanding their application range. The SASS exhibited excellent liquid resistance and could repel various composite liquids, such as milk, juice, cola, ink, ketchup, and coffee (Fig. 5(h)). These composite liquids easily slid off the SASS. When a sample was immersed in these liquids and subsequently removed, the surface remained clean without any liquid residue (Movie S4 in Appendix A). The SASS could even repel petroleum adhesion, and the petroleum could be easily removed using tweezers, which is in sharp contrast to the behavior of a pure metal that firmly adheres to its surface (Fig. S9 and Movie S5 in Appendix A). In addition to the composite liquid repellency, droplets with different pH values can easily slide off. Fig. 5(i) shows the sliding time and CA of droplets with different pH values, both of which exhibited slight changes.

Moreover, the SASS could endure high hydraulic pressure for an extended period without losing its wettability. The hydraulic pressure was measured using a visible hydraulic-testing machine. The SASS was placed in a hydraulic pressure machine for 30 days, and the CA and droplet sliding time were measured every 24 h. The CA value scarcely changed, and its values ranged from 100° to 105°, indicating that the surface wettability changed only slightly. The droplet sliding time slightly increased with time, but the droplet still slid away within 3 s on the SASS with a tilt angle of 20° after 30 days at a hydraulic pressure of 30 m (Fig. 5(j)). Moreover, the morphology of the SASS barely changed (Fig. S10 in Appendix A), and the scale armor and sliding layer remained the same as those in the original structure. This superior high hydraulic-pressure resistance makes SASS suitable for marine environments.

The corrosion resistance was quantitatively characterized using EIS (Fig. S11 in Appendix A), Tafel curves (Fig. 5(k)), and salt spray test (Fig. 5(l)). The corrosion potential (V_{corr}) value of the SASS (−0.224 V) was higher than that of pure Cu (−0.258 V). The corrosion current density (I_{corr}) value of the SASS (3.05×10^{-7} A·cm^{-2}) was lower than that of pure Cu (2.72×10^{-6} A·cm^{-2}). Details of the electrochemical corrosion results are presented in Section S3, Tables S1 and S2, and Fig. S11 in Appendix A. During the salt spray test, two samples were placed in a salt fog environment for three days, at a salt fog deposition rate of 1.67 mL·h^{-1} and NaCl concentration of 5 wt%. Pure Cu was severely corroded after three days of exposure to the salt spray, and visible corrosion marks appeared on the surface (Fig. 5(l)). In contrast, the scale armor and sliding layer of the SASS remained intact. The combination of these two structures enabled the SASS to resist the salt spray and protect the substrate from erosion (Fig. S12 in Appendix A). These results indicate that SASS exhibits significantly better corrosion resistance than pure Cu.

4. Conclusions

An SASS was fabricated via FED, which combined additive manufacturing of femtosecond laser ablation and subtractive manufacturing of electrodeposition. In the SASS structure, the scale armor grew from the substrate material and remained connected. The top of the scale was higher than the self-lubricating layer and wrapped the edges of the layer ablation holes, which became the armor of the layer. The mechanical sturdiness of the SASS relied on the femtosecond ablation ratio (f_A) of the sliding layer, which was systematically investigated in this study. Scale area ratios ranging from 0 to 30% were adopted to balance the mechanical sturdiness and slippery performance, and the optimum f_A value was 11.3%. The SASS was processed using this ratio with rectangular, triangular, and roundness scale armors. The SASS with a ratio of 11.3% could resist more than 16 000 impact cycles under an impact load of 2 MPa and withstand more than 2600 abrasion cycles under an abrasion load exceeding 1.67 MPa. This excellent mechanical sturdiness enables SASS to maintain its structural integrity and sliding performance in harsh environments. Moreover, the SASS was fabricated using FED on various metals, including Cu, Al, Ni, stainless steel, Ti, and TiNi alloys. In addition to its impressive mechanical sturdiness, SASS exhibited excellent liquid resistance, including resistance to different composite liquids and petroleum. The SASS could withstand 30 m of hydraulic pressure for 30 days without losing its antifouling performance because of its ability to cope in marine environments. Excellent corrosion resistance was demonstrated using salt spraying, EIS, and Tafel curve tests. The mechanical sturdiness and chemical durability of SASSs have considerably broadened their prospects for practical applications in antifouling and corrosion resistance. FED is currently applied to prepare SASS on many metals as a newly proposed manufacturing method. In addition to featuring a robust SASS, there is also an aspiration to broaden the

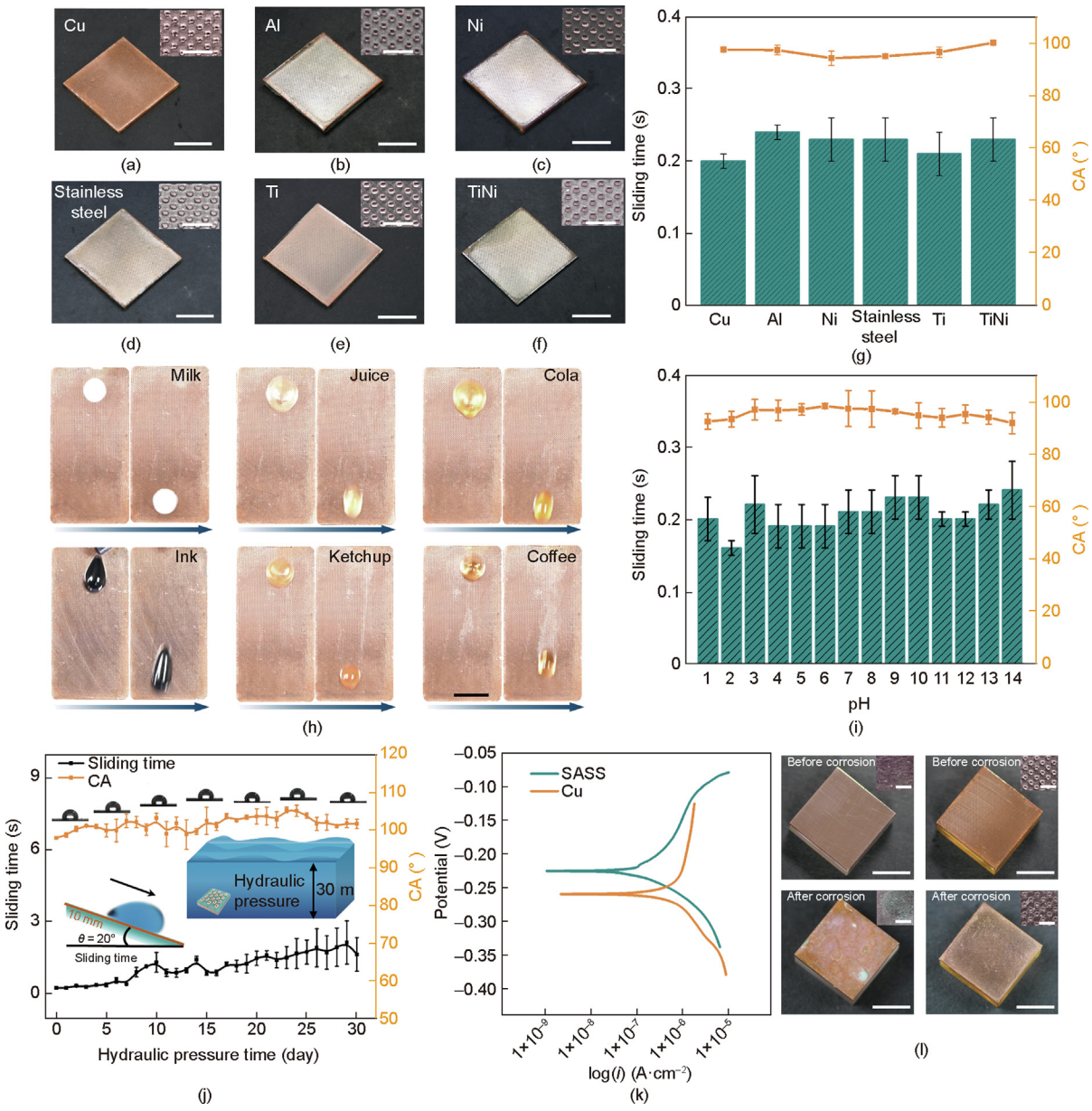

Fig. 5. Versatility of the FED method and chemical durability of SASS. (a–f) SASS fabricated using the FED method on Cu, Al, Ni, stainless steel, Ti, and TiNi alloy. Scale bar in the diagram of the structure: 500 μm; scale bar in the SASS photograph: 10 mm. (g) Wettability performance of SASS on different materials. (h) Liquid repellency of SASS using milk, juice, cola, ink, ketchup, and coffee. Scale bar: 10 mm. (i) Droplets with different pH values on SASS. (j) Hydraulic pressure resistance of SASS. (k) Tafel curves of SASS and pure Cu. *i* is the current density. (l) Morphology before and after salt fog spray on pure (left) Cu and (right) SASS. Scale bar in diagram of the structure: 500 μm; scale bar in the photograph of sample: 10 mm.

application of the FED method to the preparation of micro-nanostructures with composite surfaces featuring multiple materials to cater to droplet manipulation, underwater drag reduction and other applications.

CRediT authorship contribution statement

Jialiang Zhang: Writing – review & editing, Writing – original draft, Software, Methodology, Formal analysis, Data curation. **Qing Yang:** Writing – review & editing, Supervision, Resources, Project administration, Funding acquisition, Conceptualization. **Qingyun Ma:** Writing – review & editing, Methodology, Formal analysis, Data curation, Conceptualization. **Fangzheng Ren:** Writing – review & editing, Software, Methodology. **Yang Cheng:** Writing – review & editing. **Xiaodan Gou:** Writing – review & editing, Software, Data curation, Conceptualization. **Jie Liang:** Visualization, Investigation, Data curation. **Feng Chen:** Writing – review & editing, Visualization, Supervision, Project administration, Funding acquisition.

Declaration of competing interest

The authors declare that they have no known competing financial interests or personal relationships that could have appeared to influence the work reported in this paper.

Acknowledgments

This work was supported by the National Science Foundation of China (12127806 and 62175195), and the International Joint Research Laboratory for Micro/Nano Manufacturing and Measurement Technologies.

Appendix A. Supplementary data

Supplementary data to this article can be found online at https://doi.org/10.1016/j.eng.2024.09.026.

References

[1] Akat E, Yenmiş M, Pombal MA, Molist P, Megías M, Arman S, et al. Comparison of vertebrate skin structure at class level: a review. Anat Rec 2022;305(12):3543–608.
[2] Vernerey FJ, Barthelat F. On the mechanics of fishscale structures. Int J Solids Struct 2010;47(17):2268–75.
[3] Lin YS, Wei CT, Olevsky EA, Meyers MA. Mechanical properties and the laminate structure of Arapaima gigas scales. J Mech Behav Biomed Mater 2011;4(7):1145–56.
[4] Szewciw L, Barthelat F. Mechanical properties of striped bass fish skin: evidence of an exotendon function of the stratum compactum. J Mech Behav Biomed Mater 2017;73:28–37.
[5] Duan T, Wang J, Guo Y, Xu X, Wang D, Zheng W, et al. Characterization of the cross-structure and composition of crucian fish scales. Chin J Tissue Eng Res 2018;22:4191–5. Chinese.
[6] Tesler AB, Prado LH, Thievessen I, Mazare A, Schmuki P, Virtanen S, et al. Nontoxic liquid-infused slippery coating prepared on steel substrates inhibits corrosion and biofouling adhesion. ACS Appl Mater Interfaces 2022;14(25):29386–97.
[7] Lv S, Zhang X, Yang X, Liu Q, Liu X, Yang Z, et al. Slippery surface with honeycomb structures for enhancing chemical durability of aluminum. Colloids Surf A Physicochem Eng Asp 2022;648:129187.
[8] Liang Y, Wang P, Zhang D. Designing a highly stable slippery organogel on Q235 carbon steel for inhibiting microbiologically influenced corrosion. ACS Appl Bio Mater 2021;4(8):6056–64.
[9] Zheng Z, Guo Z, Liu W, Luo J. Low friction of superslippery and superlubricity: a review. Friction 2023;11(7):1121–37.
[10] He Z, Mu L, Wang N, Su J, Wang Z, Luo M, et al. Design, fabrication, and applications of bioinspired slippery surfaces. Adv Colloid Interface Sci 2023;318:102948.
[11] Agarwal H, Quinn LJ, Walter SC, Polaske TJ, Chang DH, Palecek SP, et al. Slippery antifouling polymer coatings fabricated entirely from biodegradable and biocompatible components. ACS Appl Mater Interfaces 2022;14(15):17940–9.
[12] Chen H, Zhang P, Zhang L, Liu H, Jiang Y, Zhang D, et al. Continuous directional water transport on the peristome surface of *Nepenthes alata*. Nature 2016;532:85–9.
[13] Wong TS, Kang SH, Tang SKY, Smythe EJ, Hatton BD, Grinthal A, et al. Bioinspired self-repairing slippery surfaces with pressure-stable omniphobicity. Nature 2011;477(7365):443–7.
[14] Wang N, Xiong D, Pan S, Wang K, Shi Y, Deng Y. Robust superhydrophobic coating and the anti-icing properties of its lubricants-infused-composite surface under condensing condition. New J Chem 2017;41(4):1846–53.
[15] Yu M, Liu M, Hou Y, Fu S, Zhang L, Li M, et al. Covalently grafted liquids for transparent and omniphobic surfaces via thiol-ene click chemistry. J Mater Sci 2020;55(27):12811–25.
[16] Yong J, Chen F, Yang Q, Du G, Bian H, Zhang D, et al. Rapid fabrication of large-area concave microlens arrays on PDMS by a femtosecond laser. ACS Appl Mater Interfaces 2013;5(19):9382–5.
[17] Yong J, Yang Q, Hou X, Chen F. Nature-inspired superwettability achieved by femtosecond lasers. Ultrafast Science 2022;2022:9895418.
[18] Zhang D, Chen F, Yang Q, Si J, Hou X. Mutual wetting transition between isotropic and anisotropic on directional structures fabricated by femotosecond laser. Soft Matter 2011;7(18):8337.
[19] Huang Z, Chen C, Wang X, Li R, Bian Y, Zhu S, et al. Light-driven locomotion of underwater bubbles on ultrarobust paraffin-impregnated laser-ablated Fe_3O_4-doped slippery surfaces. ACS Appl Mater Interfaces 2021;13(7):9272–80.
[20] Han K, Heng L, Zhang Y, Liu Y, Jiang L. Slippery surface based on photoelectric responsive nanoporous composites with optimal wettability region for droplets' multifunctional manipulation. Adv Sci 2019;6(1):1801231.
[21] Hao L, Jiang R, Gao J, Xu J, Tian L, Zhang X, et al. Metal–organic framework (MOF)-based slippery liquid-infused porous surface (SLIPS) for purely physical antibacterial applications. Appl Mater Today 2022;27:101430.
[22] Cheng Y, Yang Z, Gou X, Yang Q, Zhang Z, Cui S, et al. Heart valve-inspired self-lubricating anticoagulant surfaces. Chem Eng J 2023;474:145358.
[23] Han D, Zhang Y, Chen Z, Li J, Ma J, Mao J, et al. Carnivorous plants inspired shape-morphing slippery surfaces. Opto-Electron Adv 2023;6(1):210163.
[24] Yan T, Ji L, Li J, Zhao P, Ma X. Tailoring surface wettability of TZP bioceramics by UV picosecond laser micro-fabrication. Appl Phys A 2018;124(2):97.
[25] Chen L, Huang S, Ras RHA, Tian X. Omniphobic liquid-like surfaces. Nat Rev Chem 2023;7(2):123–37.
[26] Samaha MA, Gad-el-Hak M. Slippery surfaces: a decade of progress. Phys Fluids 2021;33(7):071301.
[27] Ouyang Y, Kang H, Guo E, Qiu R, Su K, Chen Z, et al. Thermo-driven oleogel-based self-healing slippery surface behaving superior corrosion inhibition to Mg–Li alloy. J Magnes Alloy 2023;11(12):4710–23.
[28] Cheng Y, Yang Q, Lu Y, Yong J, Fang Y, Hou X, et al. A femtosecond Bessel laser for preparing a nontoxic slippery liquid-infused porous surface (SLIPS) for improving the hemocompatibility of NiTi alloys. Biomater Sci 2020;8(23):6505–14.
[29] Xing K, Li Z, Wang Z, Qian S, Feng J, Gu C, et al. Slippery coatings with mechanical robustness and self-replenishing properties as potential application on magnesium alloys. Chem Eng J 2021;418:129079.
[30] Zhang M, Chen R, Liu Q, Liu J, Yu J, Song D, et al. Long-term stability of a liquid-infused coating with anti-corrosion and anti-icing potentials on Al alloy. ChemElectroChem 2019;6(15):3911–9.
[31] Sun L, Wang Y, Zhang X, Bian F, Shang L, Zhao Y, et al. Bio-inspired self-replenishing and self-reporting slippery surfaces from colloidal co-assembly templates. Chem Eng J 2021;426:131641.
[32] Wang X, Bai H, Li Z, Cao M. Fluid manipulation via multifunctional lubricant infused slippery surfaces: principle, design and applications. Soft Matter 2023;19(4):588–608.
[33] Gulfam R, Zhang P. Power generation and longevity improvement of renewable energy systems via slippery surfaces—a review. Renew Energy 2019;143:922–38.
[34] Chen X, Wen G, Guo Z. What are the design principles, from the choice of lubricants and structures to the preparation method, for a stable slippery lubricant-infused porous surface? Mater Horiz 2020;7(7):1697–726.
[35] Fang Y, Yong J, Huo J, Yang Q, Cheng Y, Liang J, et al. Bioinspired slippery surface fabricated by femtosecond laser and its applications. Laser Optoelectron Prog 2020;57:151–69. Chinese.
[36] Xiang H, Yuan Y, Zhang C, Dai X, Zhu T, Song L, et al. Key factors affecting durable anti-icing of slippery surfaces: pore size and porosity. ACS Appl Mater Interfaces 2023;15(2):3599–612.
[37] Sung C, Heo Y. Porous layer-by-layer films assembled using polyelectrolyte blend to control wetting properties. Polymers 2021;13(13):2116.
[38] Li X, Zhang D, Liu Z, Li Z, Du C, Dong C. Materials science: share corrosion data. Nature 2015;527(7579):441–2.
[39] Lee J, Lee MH, Choi CH. Design of robust lubricant-infused surfaces for anti-corrosion. ACS Appl Mater Interfaces 2022;14(1):2411–23.
[40] Gu H, Wang H, Zhu S, Yuan D, Dai X, Wang Z. Interspecific differences and ecological correlations between scale number and skin structure in freshwater fishes. Curr Zool 2023;69(4):491–500.
[41] Sveen L, Karlsen C, Ytteborg E. Mechanical induced wounds in fish—a review on models and healing mechanisms. Rev Aquacult 2020;12(4):2446–65.
[42] Wang S, Wang S, Xue Y, Xue Y, Liu Q, Cao L, et al. Durable nanofluids-infused hierarchical surfaces with high corrosion and abrasion resistance. Adv Eng Mater 2023;25(8):2201292.
[43] Gurav AB, Shi H, Duan M, Pang X, Li X. Highly transparent, hot water and scratch resistant, lubricant-infused slippery surfaces developed from a mechanically-weak superhydrophobic coating. Chem Eng J 2021;416:127809.
[44] Yuan S, Peng J, Zhang X, Lin D, Geng H, Han B, et al. A mechanically robust slippery surface with 'corn-like' structures fabricated by *in-situ* growth of TiO_2 on attapulgite. Chem Eng J 2021;415:128953.
[45] Zhu Y, He Y, Yang DQ, Sacher E. A facile method to prepare mechanically durable super slippery polytetrafluoroethylene coatings. Colloids Surf A 2018;556:99–105.
[46] Baidya A, Das SK, Pradeep T. An aqueous composition for lubricant-free, robust, slippery, transparent coatings on diverse substrates. Glob Chall 2018;2(2):1700097.
[47] Gao X, Guo Z. Mechanical stability, corrosion resistance of superhydrophobic steel and repairable durability of its slippery surface. J Colloid Interface Sci 2018;512:239–48.
[48] Zhang B, Xu W, Zhu Q, Guan F, Zhang Y. Nepenthes pitcher-inspired lubricant-infused slippery surface with superior anti-corrosion durability, hot water repellency and scratch resistance. J Ind Eng Chem 2022;107:259–67.
[49] Fan H, Guo Z. Robust multi-functional slippery surface with hollow ZnO nanotube structures. New J Chem 2020;44(36):15483–91.
[50] Yang J, Zhang Y, Jia X, Chen B, Li Y, Wang S, et al. A mechanically robust slippery coating for anti-corrosion, photothermal deicing, and anti-sticking applications. Surf Coat Tech 2022;438:128395.
[51] He J, Wang J, Wang R, Jie J, Chen B, Luo G, et al. Preparation and anti-icing performance of liquid lubricant micro-nano composite coating based on modified nano-SiO_2. J Adhes Sci Technol 2023;37(14):2139–53.